HHS Public Access

Author manuscript

Phys Med Biol. Author manuscript; available in PMC 2016 November 07.

Published in final edited form as:

Phys Med Biol. 2015 November 7; 60(21): 8457–8479. doi:10.1088/0031-9155/60/21/8457.

Computer-aided Detection System for Clustered Microcalcifications in Digital Breast Tomosynthesis using Joint Information from Volumetric and Planar Projection Images

Ravi K Samala, **Heang-Ping Chan**, **Yao Lu**, **Lubomir M Hadjiiski**, **Jun Wei**, and **Mark A Helvie**

Department of Radiology, University of Michigan, Ann Arbor, Michigan 48109-5842

Abstract

We propose a novel approach for detection of microcalcification clusters (MCs) using joint information from digital breast tomosynthesis (DBT) volume and planar projection (PPJ) image. A data set of 307 DBT views was collected with IRB approval using a prototype DBT system. The system acquires 21 projection views (PVs) from a wide tomographic angle of 60° (60°-21PV) at about twice the dose of a digital mammography (DM) system, which allows us the flexibility of simulating other DBT acquisition geometries using a subset of the PVs. In this study, we simulated a 30° DBT geometry using the central 11 PVs (30°-11PV). The narrower tomographic angle is closer to DBT geometries commercially available or under development and the dose is matched approximately to that of a DM. We developed a new joint-CAD system for detection of clustered microcalcifications. The DBT volume was reconstructed with a multiscale bilateral filtering regularized method and a PPJ image was generated from the reconstructed volume. Task-specific detection strategies were designed to combine information from the DBT volume and the PPJ image. The data set was divided into a training set (127 views with MCs) and an independent test set (104 views with MCs and 76 views without MCs). The joint-CAD system outperformed the individual CAD systems for DBT volume or PPJ image alone; the differences in the test performances were statistically significant ($p<0.05$) using JAFROC analysis.

Keywords

digital breast tomosynthesis; computer-aided detection; microcalcification; multiscale enhancement; regularized reconstruction; planar projection image

I. INTRODUCTION

Computer-aided detection (CAD) for digital breast tomosynthesis (DBT) has been developed to detect microcalcification clusters (MCs) in the reconstruction volume or slices and/or the projection views (PVs). Detection on PVs has the advantage of being independent of reconstruction method while detection in the reconstructed volume has the advantage of having higher contrast-to-noise ratio (CNR) for microcalcifications after all projections are combined. In this study, we attempt to tackle the problem in the reconstruction domain by

rsamala@med.umich.edu

joint detection in the reconstructed volume and a planar projection (PPJ) image generated from the reconstructed volume.

DBT acquired with different prototype systems were used for preliminary studies of CAD for MC detection. Reiser *et al* (Reiser *et al.*, 2008) used 60 DBT views (30 with MCs and 30 without MCs) from a GE prototype DBT acquiring 11 PVs within a 50° tomographic angle in a step-and-shoot mode and achieved a sensitivity of 86% at 1.3 FPs/view. Park *et al* (Park *et al.*, 2008) achieved 70% sensitivity at 4 FPs/view and 88% sensitivity at 15.9 FPs/view for detection in PVs and DBT volume, respectively, in a data set of 96 DBT views from a Hologic experimental DBT system that acquired 11 PVs. Bernard *et al* (Bernard *et al.*, 2008) reported a sensitivity of 85% at 1.4 FPs/view using a data set of 50 DBT views (13 with MCs, 37 without MCs) from a GE prototype DBT system based on a Senographe DS FFDM system that acquired 15 PVs over a 40° tomographic angle. van Schie *et al* (van Schie and Karssemeijer, 2009) achieved a sensitivity of 95% at 1.5 FPs/view in a data set of 41 views (12 with MCs, 29 without MCs) acquired with a Sectra photon-counting prototype DBT system having 24° and 12° tomographic angles. In our laboratory, a GE GEN2 prototype DBT system acquiring 21 PVs over a 60° tomographic angle was used for collecting DBT cases. We have been developing methods to detect MCs in DBT (Sahiner *et al.*, 2012; Samala *et al.*, 2014c), PVs (Wei *et al.*, 2014), and PPJ image (Samala *et al.*, 2014b). Our CAD systems achieved 85% sensitivity at 2.16 FPs/view in DBT volume, 90% sensitivity at 1.55 FPs/view in PVs, and 85% sensitivity at 0.71 FPs/view in PPJ images. The study on DBT and PPJ was tested on an independent set of 180 views (104 with MCs, 76 without MCs) and the detection on PVs was evaluated by cross-validation using 82 DBT views with MCs. For the same DBT system, Xu *et al* (Xu *et al.*, 2014) used a two pronged approach by combining the predictions from a random-forest classifier and a rule-based classifier. The rule-based classifier was designed to enhance segmentation by combining median filtering with graph-cut-based segmentation.

Population-based studies comparing lesion detection by radiologists in DM with that in combined DM and DBT have shown improved detection of invasive cancers and reduction of recalls (Skaane *et al.*, 2013b; Skaane *et al.*, 2013a; Ciatto *et al.*, 2013; McCarthy *et al.*, 2014). With the approval of three commercial DBT systems by the Food and Drug Administration in the United States (Chakrabarti *et al.*; Food and Drug Administration August 2014; Food and Drug Administration April 2015), implementation of DBT continues to increase in clinical practice. CAD has the potential to assist radiologists in detecting MCs in DBT, which has been reported to be more challenging than detection in DM in some studies (Poplack *et al.*, 2007; Spangler *et al.*, 2011). We have been developing CAD methods using reconstructed DBT volume (CAD_{DBT}) and PPJ image (CAD_{PPJ}) independently as input for a wide tomographic angle (60°) DBT system (fig. 1(a)). CAD_{PPJ} was designed to take advantage of the improved CNR and the reduction in search space over the detection in the DBT volume. It was shown to have better performance than CAD_{DBT} and the difference was statistically significant.

We have been collecting DBT images of human subjects using a prototype DBT system. The system acquires 21 projection views (PVs) with a wide tomographic angle of 60° (fig. 1(a)). The total dose per view is set up to be about twice the dose of a digital mammogram

(DM) of the same view. The system thus has wider tomographic angle and provides more PVs than most of the systems commercially available or under development (11° - 50°, 13 - 25 PVs) (Sechopoulos, 2013). Therefore, our data set offers us the flexibility of using a subset of the PVs to simulate some other DBT acquisition geometries for research purposes (Lu *et al.*, 2011b; Samala *et al.*, 2014a). In the current study, we simulated a narrow-angle DBT system by using the central 11 PVs (fig. 1(b)) from the original DBT scan acquired with our 60°, 21 PV system. A multiscale bilateral filtering regularized simultaneous algebraic reconstruction technique (Lu *et al.*, 2015) was employed to reconstruct the DBT volume and generated a PPJ image. We designed a joint-CAD system that combined the information from the DBT reconstructed volume and the corresponding PPJ image for microcalcification detection, and compared its performance to those of the individual CAD_{DBT} and CAD_{PPJ} systems. As reference, we also compared the detection in the DBT at 30°, 11 PVs to our previous results in the higher dose DBT at 60°, 21 PVs.

II. MATERIALS AND METHODS

II. A. DBT geometry and reconstruction

A General Electric GEN2 prototype DBT system was used to acquire 21 PVs at 3° intervals covering a wide angular range of 60° (fig. 1(a)). The prototype DBT system uses a step-and-shoot design with the x-ray source and the detector stationary during exposure. The total scan time takes less than 8 seconds. The system has a Rh-anode/Rh-filter x-ray tube and a flat panel CsI/a:Si detector with a pixel pitch of 0.1 mm × 0.1 mm. The imaging techniques of the system were set up such that the total mean glandular dose for each DBT scan (21 PVs) was about two times of that of a single digital mammogram of a GE Essential digital mammography system for a similar breast.

From the data set acquired with the 60°, 21 PV geometry, we simulated a narrow 30° tomographic angle with 11 PVs at 3° intervals (fig. 1(b)). The narrow-angle geometry would be closer to those used for most current and future DBT systems (Sechopoulos, 2013) and the dose would also be close to the target of keeping the radiation exposure of DBT about the same as 2D mammography. For the rest of the discussion these two geometries are referred to as 60°-21PV and 30°-11PV, respectively.

The simultaneous algebraic reconstruction technique (SART) (Zhang *et al.*, 2006) with multiscale bilateral filtering (MSBF) regularization (Lu *et al.*, 2015) is used for DBT reconstruction with a slice spacing of 1 mm and an in-plane resolution of 0.1 mm × 0.1 mm. Regularization during the reconstruction was shown to improve CNR of microcalcifications when selectively applied to different categories of pixels (Lu *et al.*, 2010; Lu *et al.*, 2011a). MSBF-regularized SART (Lu *et al.*, 2015) improves the CNR of microcalcifications while preserving the sharpness of microcalcifications and spiculated masses and the image quality of the background tissue. In this method, the DBT slices are decomposed into multiscale structure using Laplacian pyramid decomposition after each iteration of SART reconstruction. The decomposed high-frequency component is denoised using MSBF with optimized domain and range filter kernels. The pyramid is then recomposed and fed back to SART for the next iteration. At the final iteration of reconstruction, DBT slices containing both soft tissue structured background and enhanced microcalcifications are output. In

addition, a PPJ image is generated by maximum intensity projection of the high-frequency components in the Laplacian pyramids of the stack of DBT slices along the z-direction perpendicular to the detector plane. The resulting PPJ image contains microcalcifications and high-frequency structures such as fibrous tissue edges or metallic artifacts but without background structured information. During the maximum intensity projection, the original z location of the voxel that has the maximum intensity value in the DBT volume is recorded on a "z-map" for each pixel on the PPJ image.

II. B. Data set

With Institutional Review Board (IRB) approval and written informed consent, we obtained two-viewed DBT (craniocaudal (CC) and mediolateral oblique (MLO) views) from breasts of patients in the Department of Radiology at the University of Michigan Health System. All cases were assessed as BI-RADS 4 and BI-RADS 5 and recommended for biopsy. One hundred fifty-four cases were used in this study, of which 34 clusters were biopsy-proven to be malignant and 82 were benign. The rest contained soft tissue lesions that were biopsy-proven to be benign and were used as cases without MCs ("normal" with respect to MC). The data set of 307 views (one of the 308 views was lost due to technical failure) was partitioned into a training set and an independent test set by case so that all views of the same case were always assigned to the same set. The training set contained 127 views from 64 breasts with MCs and the test set contained 104 views from 52 breasts with MCs and 76 views from 38 breasts without MCs. An MQSA-approved radiologist marked the microcalcification cluster with a 3-dimensional (3D) box in the DBT volume using all available clinical mammograms and biopsied markers as reference. The radiologist marked a total of 124 clusters on the 127 views in the training set and 100 clusters on the 104 views on the test set. For three breasts in the training set and 4 breasts in the test set, the MC was visible only in one of the views. The radiologist also provided BI-RADS density category of the breast and a subtlety rating for each marked cluster. The distributions of the breast density and the subtlety ratings of the clusters in the entire data set can be found in our previous work (Samala *et al.*, 2014b). Table 1 and fig. 2 present the characteristics of the data set partitioned into training and test sets. Between the two sets, the BI-RADS breast density is comparable, but with very few malignant cases in the test set, the training set has more clusters with higher visibility ratings of 1 to 3.

II. C. CAD for DBT and PPJ

The CAD systems for the 60°-21PV geometry based on the DBT reconstructed volume and the PPJ image were developed and described in detail previously (Samala *et al.*, 2014b; Samala *et al.*, 2014c). These CAD systems were applied to the 60°-21PV data set and the 30°-11PV data set. The joint-CAD system is designed using these two CAD systems as foundation. In the following, a brief overview of the CAD_{DBT} and CAD_{PPJ} systems is given first, followed by more detailed description of the strategies of combining the DBT and PPJ information.

II. C. 1 CAD system for DBT (CAD_{DBT})—The reconstructed DBT volume resulting from the SART reconstruction with MSBF regularization is processed to generate a multiscale calcification response volume and a CNR enhanced volume that emphasize the

structure and the contrast properties of microcalcifications, respectively. These responses are combined to generate an enhancement-modulated calcification response (EMCR) volume in which seed objects are detected as microcalcification candidates. An iterative process that combines thresholding and region growing of the EMCR volume generates *N* objects. The microcalcification candidates are extracted from the image background with a locally adaptive segmentation of these objects. Three CNR thresholds are determined adaptively based on an analysis of the CNR histogram of the candidates from each volume to stratify subtle to obvious microcalcifications. With a dynamic conditional clustering algorithm starting from high to low ranking of the *N* objects, an initial set of clusters is obtained using CNR threshold and distance criteria. The CNR threshold in combination with the size and the number of candidates in a cluster provides decision criteria for further FP reduction. The final clusters are detected after imposing additional FP reduction steps based on the shape of the cluster and maximum intensity projection of the 3-dimensional cluster to exclude linear objects and linear shaped clusters that may represent vascular calcifications.

II. C. 2 CAD system for PPJ (CAD_{PPJ})—The PPJ image is generated by maximum intensity projection from the MSBF-regularized high-frequency components of the DBT slices at the final iteration of reconstruction. It thus contains only high-frequency structures including microcalcifications and noise. Note that the PPJ image is similar to a background- or low-frequency-subtracted 'synthetic' image. In the CAD_{PPJ} system, the top *N* locations are identified directly from the PPJ image in analogy to the process described in CAD_{DBT}. They are then screened by a trained convolution neural network (CNN) (Ge *et al.*, 2006; Gurcan *et al.*, 2002; Gurcan *et al.*, 2001) to classify microcalcification-like objects from tissue structures and artifacts. The remaining microcalcification candidates are segmented by region growing using a locally adaptive threshold for each individual object. By analysis of the CNR histogram of the segmented objects, CNR thresholds that stratify microcalcifications of different degrees of subtlety are estimated. The CNR thresholds, in combination with the size and the number of calcifications, are used for FP reduction and dynamic conditional clustering. For the data set of 60°-11PV geometry, it was observed that the CNR feature of the objects in the PPJ images provides better TP and FP differentiation compared to that in DBT, resulting in better overall MC detection performance (Samala *et al.*, 2014b).

II. D. Joint-CAD for 30°-11PV geometry

The joint-CAD system incorporates the individual steps from each of the CAD_{DBT} and CAD_{PPJ} systems within one framework with task-specific strategies to take advantage of the combined information. The joint-CAD system can be broadly divided into three stages: (i) preprocessing of the DBT volume, generation of microcalcification candidates and cluster candidates in DBT and PPJ (fig. 3(a)), (ii) FP reduction of clusters (fig. 3(b)), and (iii) mapping of clusters from the DBT domain to the PPJ domain (fig. 4). These steps are described in detail in the following sections.

II. D. 1. Reconstruction of DBT and Generation of PPJ—In our previous study, the number of iterations, relaxation parameter sequence and kernel size of the domain filter for MSBF regularization during the SART reconstruction were optimized for the 60°-21PV

system (Lu *et al.*, 2015). The number of iterations was chosen to be two, the relaxation parameter sequence was 0.5 and 0.3, and the standard deviation of the Gaussian domain filter was set at 3 pixels. The standard deviation of the range filter was adaptively calculated from the noise variance of the DBT volume being reconstructed. For the 30°-11PV system, we have investigated the potential effects of the number of iterations, the relaxation parameter sequence and domain filter kernel on CAD performance (Samala *et al.*, 2014a). The number of iterations was found to be the most important parameter to adjust for the lower dose DBT. A medical physicist experienced in mammography marked 301 individual microcalcifications in nine selected clusters in the DBT volumes as TPs. These views were chosen because they provided a large number of microcalcifications within a small number of volumes so that the optimization of reconstruction parameters based on microcalcification properties could be performed efficiently. None of these 9 views belonged to the test set. The TP locations were projected to the corresponding PPJ image to identify the TPs on PPJ. The microcalcification candidates from the top N locations during the candidate prescreening step for DBT (or PPJ), excluding those overlapping with the TPs, were considered to be FPs. The TPs and FPs from each type of images formed a training set for the following analysis. Three parameters were calculated from the CNR of these locations: the mean CNR of the microcalcifications (μ_m), the mean CNR of the FPs (μ_n), and the area under the receiver operating characteristic curve (AUC) calculated from the CNR distribution of the two classes fitted with a binormal model using the ROC analysis program (ROC library 1.0.3 v 2011, URL: http://xray.bsd.uchicago.edu/krl/) by Metz *et al.* (Metz and Pan, 1999). The selection of the iteration number is based on two figures-of-merit (FOMs): the AUC and the adjusted mean ($\mu_m - \mu_n$) as plotted in fig. 5. The AUC assesses the ability of the CNR values to discriminate between the TP and FP candidates and the adjusted mean quantifies the separation between the two classes. On this plot, the performance of the 60°-21PV system is considered the target to be achieved for the lower dose system, i.e., the closer the FOMs for the lower dose set are to the higher dose set, the better the expected performance of the CAD system. For DBT, iteration 2 has higher AUC and lower adjusted mean compared to iteration 3. Iterations 4 and 5 have lower $AUCs$ and adjusted means than iteration 3. Our CAD system employs both object-based features (related to AUC) and cluster-based features (related to adjusted mean) for FP reduction. However, the dynamic conditional clustering benefits more on a higher adjusted mean. Iteration 3 was therefore selected although it attains a lower AUC than iteration 2. For PPJ, the AUC and adjusted mean decrease monotonically from iteration 2 to iteration 5. Hence, iterations 3 and 2 were chosen for DBT and PPJ, respectively. For the 60°-21PV geometry, iteration 2 was chosen for both the CAD_{DBT} and the CAD_{PPJ} systems in previous studies.

II. D. 2. Cluster detection—In the joint-CAD system, prescreening of cluster candidates consists of two paths, one in the DBT volume and the other in the PPJ image (fig. 3(a)), which follow the same methods as those in the CAD_{DBT} and the CAD_{PPJ} systems (Section II.C) (Samala *et al.*, 2014b; Samala *et al.*, 2014c), respectively. Both start from identifying N objects with top CNR ranking as cluster seeds, from which cluster candidates are formed by a dynamic conditional clustering algorithm that imposes criteria on the characteristics of the microcalcification candidates (CNR thresholds, CNR ranking and distance) in a dynamic clustering process. The criteria are designed differently for the DBT and the PPJ paths and

are adaptive to the individual cases. The PPJ path has one additional step of object-based FP reduction that involves: (a) CNN based threshold for the top *N* objects, and (b) classifying an object as FP if the EMCR value in the DBT volume corresponding to the centroid location of the object is zero, where the voxel location in the DBT volume corresponding to the pixel is determined from the z-map for the PPJ image. The initial sets of clusters from the two paths are then passed onto the next step for further FP reduction.

Even with dynamic conditional clustering where a cluster grows from a starting seed location to include microcalcifications over a region, the resulting clusters can still be only a part of the entire cluster and results in multiple TP clusters within each DBT volume or PPJ image. This occurs when a cluster that includes loosely grouped microcalcifications spreads out in a relatively wide region. The fragmentation of the cluster is random and it depends on the starting centroid location of the cluster and the direction of cluster growth, which is controlled by the CNR ranking of the microcalcification candidates. Therefore, there can be multiple TP clusters within each view. The overlap and non-overlap cluster analyses are performed at this stage. The total number of TP clusters in these intermediate steps will be larger than the number of clusters marked by the radiologist in the data set.

II. D. 3. False positive reduction—After the dynamic clustering stage from DBT and PPJ paths, the clusters are aggregated in the cluster pool. The clusters are categorized into three types: detected only in DBT, only in PPJ, and in both DBT and PPJ (DBT∩PPJ) as shown in fig, 3(b). To determine if a cluster detected in the DBT path overlaps with a cluster detected on the PPJ image, the DBT cluster is projected onto the PPJ image. If the centroid of the DBT cluster falls within the bounding box of a PPJ cluster or vice versa, the two clusters are considered overlapped. If more than one DBT clusters overlap with the PPJ cluster, the DBT cluster with the highest CNR score is kept while the other DBT clusters will be considered FPs. This will reduce the number of low score clusters that are more likely to be FPs to be passed from the DBT volume to the cluster pool.

Three different linear discriminant analysis classifiers (LDA_i, i=1,2,3) were trained. LDA_1 and LDA_3 were trained on the set of DBT or PPJ cluster features, respectively. LDA_2 was trained on the cluster features that were aggregated from the (DBT∩PPJ) clusters. Each feature set had 21 morphological features (Chan *et al.*, 1998) for the DBT (or PPJ) clusters, including the number of microcalcification candidates within the cluster and 20 cluster features derived as the mean, standard deviation, coefficient of variation, and maximum from each of 5 morphological features (the area, mean density, eccentricity, moment ratio and axis ratio) of the individual objects in a cluster. For the PPJ clusters, the feature set had four additional CNN features (Ge *et al.*, 2006) derived as the average of the three highest CNN scores and the mean, minimum, and maximum of the CNN scores of all objects in the cluster. Stepwise LDA method for feature selection and classification using *F*-statistics based thresholds and correlation tolerance parameter were used to search for the best features and weights for the FP classifier, as described in our previous studies (Chan *et al.*, 1998; Way *et al.*, 2010). The LDA was trained with a leave-one-case-out cross-validation method from the 127 training views. The discriminant scores generated from the LDA classifiers were passed to a decision tree classifier. Note that during the training of LDA_1, all the DBT clusters were used in the leave-one-case-out cross-validation to have a large data

sample, but only the scores of the DBT clusters that do not overlap with the PPJ clusters (DBT\PPJ) in this path are passed onto the next step. This is a bias explicitly introduced into the joint-CAD system due to PPJ having better class separation than DBT. By removing the DBT∩PPJ clusters from the LDA_1 path, the decision tree classifier will have a missing feature and thus depend more on the features from the LDA_2 and LDA_3. This approach also results in a smaller decision tree structure that reduces the chance of overtraining.

Combining the clusters from both the DBT and PPJ paths results in increased sensitivity and also potentially doubling the FPs. Our previously developed FP reduction rules based on CNR, and the size and number of candidates in a cluster for the individual CAD_{DBT} and CAD_{PPJ} systems are not effective with such a large increase in FPs. We therefore trained a decision tree classifier using the LDA scores of a total of 2304 clusters (489 TPs and 1815 FPs) from the three types of clusters in the training set. The total number of TP clusters was larger than the number of views in the training set due to the fragmentation of clusters as mentioned in Section II.D.3. The J48 classification algorithm from WEKA (Hall *et al.*, 2009), which is an implementation of the C4.5 decision tree classifier (Quinlan, 1993), was used with reduced error pruning to generate a decision tree. The C4.5 has the advantages of inherently handling missing values, which in this study came from clusters detected only in the PPJ or the DBT path, and that the resulting model is easily interpretable and modifiable. The purpose of the classifier at this stage is to moderately reduce the FPs in both paths while keeping the sensitivity high. Further FP reduction will be accomplished by applying the previously developed decision rules for the CAD_{DBT} and CAD_{PPJ} systems to the DBT clusters and PPJ clusters, respectively, in the second FP reduction step (fig. 3(b)).

II. D. 4 Mapping of clusters—The resulting clusters from the cascaded FP reduction steps are categorized into two groups: one contains those detected in DBT alone (i.e., DBT \PPJ) and the other contains clusters detected either in PPJ alone or both. Since the CNR feature in PPJ has better discriminatory power for TP and FP candidates compared to that in the DBT volume, the DBT\PPJ clusters are mapped to the PPJ domain, i.e., the locations of the cluster and the individual objects in the cluster are projected onto the PPJ image, and segmentation and feature extraction for the objects are performed on the PPJ image. The trained LDA_3 classifier (fig. 3(b)) is used to generate scores for these clusters, which are then aggregated into the pool of detected clusters as shown in fig. 4. The final detected PPJ clusters are compared with the radiologist-marked reference cluster locations to evaluate the performance of the joint-CAD system.

II. E. Performance evaluation

For evaluation of detection performance, the detected clusters are compared to the radiologist-marked reference box on each view. A detected cluster is counted as TP if either its centroid falls within the reference box or vice versa. In case of PPJ clusters, the radiologist-marked 3D box is projected onto the PPJ image as reference. In the final set of detected clusters, if more than one cluster with different discriminant scores overlap with one another or fall into the same reference box, the clusters are merged and the score from the merged cluster is determined as the maximum score within the merged clusters. Therefore, the number of detected clusters will not exceed the number of reference clusters.

A free response receiver operating characteristic (FROC) curve is generated by varying the decision threshold on the cluster score over the entire range and the sensitivity and FP rates are determined at each threshold.

III. RESULTS

III. A. Analysis of overlapped and non-overlapped clusters

The PPJ image is generated from maximum intensity projection of the high-frequency components of the MSBF-regularized DBT slices. This results in non-linear, relative change in the properties of microcalcifications and FPs between DBT and PPJ. The different segmentation will result in different size, shape and CNR feature values, which, in combination with the differences in the detection process, may lead to TP and FP detections of different properties. Based on these factors, DBT and PPJ may be considered different co-registered imaging modalities. Combining the detections on the reconstructed DBT and the PPJ image has twofold advantages, as discussed in Sections III.A.1 and III.A.2.

III. A. 1. Overlapped clusters—Fig. 6 shows the distribution of the CNR of the overlapped TP and FP clusters between the DBT and PPJ paths after the clustering stage (fig. 3(a)). The CNR of a cluster is defined as the maximum CNR among all member objects in that cluster. The overlapped clusters between the DBT and PPJ paths are ranked based on the CNR of the clusters. Fig. 7(a) shows the correlation in terms of CNR rankings between the two sets of clusters from the DBT path and the PPJ path as a heat map generated by the rank-rank hypergeometric overlap (RRHO) method (Plaisier *et al.*, 2010). The RRHO method determines the degree of statistical correlation using a hypergeometric distribution while a rank threshold is varied over all possible values through the two ranked lists. The correlation is quantified by the $\log_{10}$-transformed hypergeometric overlap of subsections of the DBT and PPJ cluster ranked lists. A subsection is determined by integrating the rank distribution up to a given threshold. The interpretation of the four quadrants on the resulting heat map is shown in fig. 7(b). Pixels with colder color indicate lower correlation between the two lists below a threshold and pixels with hotter color indicate higher correlation. Non-overlapped clusters are not taken into account in the RRHO method and the method does not differentiate between TP and FP clusters. For illustration, an RRHO map where the two ranked sets have perfect correlation is simulated by using the clusters from the PPJ path for both the x-axis and y-axis, resulting in a heat map with a red diagonal as shown in fig. 7(c). Figure 7(a) shows that correlated cluster regions mostly appear in the lower left quadrant, indicating significant correlation at the top of the ranked lists in the section of higher cluster CNR values from the DBT and PPJ detection paths. The upper right quadrant indicates lower correlation at the bottom of the ranked lists in the section of lower CNR values. Compared to the perfect correlation shown in fig. 7(c), the overlapped clusters are ranked differently between the two paths.

III. A. 2 Non-overlapped clusters—Detection of the non-overlapped TP clusters is the key that improves the detection sensitivity of the joint-CAD system over that of the individual CAD systems. Fig. 8 shows the TP and FP distributions of the non-overlapped clusters from each path. Compared to the overlapped clusters in Fig. 6, the FP distribution is

much higher compared to that of the TPs. Detecting these TP clusters while maintaining a low FP rate is therefore non-trivial. The results indicate that our FP reduction strategies using the combinations of LDA and decision tree were effective in differentiating the TP and FP clusters.

III. A. 3. FP reduction analysis—The LDA classifiers are trained to estimate discriminant scores for the clusters from the prescreening stage based on the characteristics of the detected clusters in the respective categories (DBT, PPJ and DBT∩PPJ). No FP reduction is performed by the individual LDA classifiers. The decision tree classifier and the rule-based classifier then reduce the FPs based on the three LDA scores. Table 2 lists the percentages of TPs and FPs for the training set after different stages of the joint-CAD system. After the two-stage classification, the FPs were reduced by 78% relative to the prescreening stage and only 2.4% of the true clusters were lost for the training set.

III. B. FROC performance

View-based and case-based FROC curves were generated for comparison. For view-based analysis, the same cluster imaged on the two views of the breast was considered to be a separate target. The sensitivity was calculated relative to the total of 124 MCs for the training set and 100 MCs for the test set. For case-based analysis, the same cluster imaged on the CC and MLO views of each breast was considered to be one target and detection of the cluster in either view or both views was counted as a true-positive. The sensitivity was calculated relative to the total of 64 MCs for the training set and 52 MCs for the test set. For the test FROC curves, the FP rates were estimated from detection in the 76 DBT views without MCs. Figures 9(a) and 9(b) show the view-based FROC curves of the joint-CAD system compared to those of the CAD_{DBT} and CAD_{PPJ} systems for detection in the 30°-11PV training and test set, respectively. Figure 10 compares the view-based FROC curve of the joint-CAD system for the 30°-11PV test set to those of the CAD_{DBT} and CAD_{PPJ} systems for the 60°-21PV test set. The view- and case-based FROC curves of the joint-CAD system for the 30°-11PV test set are shown in fig. 11. Table 3 lists the mean number of FPs per DBT volume or PPJ image from the joint-CAD system for the 30°-11PV test set at several sensitivities. Jackknife FROC (JAFROC) (Chakraborty and Berbaum, 2004) was used to assess the statistical significance for the difference in performances between the CAD systems. For the 30°-11PV geometry, the JAFROC analysis shows a significant difference ($p<0.05$) in the test FROC curves between the joint-CAD and the individual CAD_{DBT} and CAD_{PPJ} systems (Table 4). The differences in the test FROC curves between the joint-CAD for the 30°-11PV geometry and those of the individual systems for the 60°-21PV geometry (fig. 10) did not achieve statistical significance by JAFROC analysis ($p=0.31$ for joint-CAD vs CAD_{DBT} and $p=0.12$ for joint-CAD vs CAD_{PPJ}). Figure 12 shows the view-based FROC curve of the joint-CAD system for the 30°-11PV test set compared to the FROC curves for the CC and MLO views separately generated from the same test set. JAFROC analysis shows the difference in the figure-of-merit between the CC and MLO curves did not achieve statistical significance ($p=0.55$).

IV. DISCUSSION

The image quality of microcalcifications in DBT is affected by a number of factors (Chan *et al.*, 2014; Lu *et al.*, 2011b; Sechopoulos, 2013). The total exposure from the PVs of a DBT scan and the tomographic angle are major factors influencing the CNR of microcalcifications. We simulated a narrow-angle DBT by reducing the number of PVs to about half. If the CAD systems previously developed for 60°-21PV DBTs were applied to the 30°-11PV DBTs, the detection performance decreases, demonstrating that noise is a major factor that will affect the detectability of microcalcifications in DBT. The joint-CAD system incorporated with new task-specific strategies is designed to exploit the information from both the reconstructed DBT volume and the corresponding PPJ image, with a goal to improve the performance.

It is expected that there will be an increased sensitivity by combining the detection results due to the non-overlapped true clusters between the DBT and PPJ detection paths as shown in fig.8. Figure 13 shows two examples of non-overlapped clusters from the training set. It is also possible to achieve a better FROC curve, i.e., higher sensitivity at all possible FP rates, given that the overlapped true clusters were ranked differently and its final ranking improved among all cluster candidates. This is shown in fig. 7 by the RRHO plot indicating the difference in ranking of the overlapped clusters. On the other hand, combining the detected clusters from the DBT and PPJ paths would also increase the FPs by approximately two folds if there were no effective FP reduction strategies. Although the development of the joint-CAD system has its foundation on the CAD_{DBT} and CAD_{PPJ} approaches, changes were implemented to counter the increase in FP rate. The major differences between the joint-CAD system and the CAD_{DBT} and CAD_{PPJ} systems include: (a) A new approach to identify the optimal combination of SART iteration based on the *AUC* and the adjusted mean of TP and FP candidates. (b) The overlapped and non-overlapped clusters are stratified and three LDA classifiers are trained to generate cluster-based discriminant scores from the morphological and CNN features of microcalcifications. (c) A decision tree classifier is used as an FP reduction step based on the LDA scores. (d) The DBT clusters are mapped onto the PPJ image and cluster discriminant scores for the mapped PPJ clusters are also generated using the LDA_3 classifier specifically trained for PPJ features.

The FROC plots in fig. 9(a) for the training set in a 30°-11PV geometry increased the maximum sensitivity from 90% for both CAD_{DBT} and CAD_{PPJ} to 97% for the joint-CAD approach. At 90% view-based sensitivity, the FP rate was 1.4 FPs/view by the joint-CAD system compared to 2.96 and 2.76 FPs/view by the CAD_{DBT} and CAD_{PPJ} systems, respectively. For the test set (fig.9(b)), the joint-CAD achieved a maximum sensitivity of 89% at 2.9 FPs/view compared to 74% and 79% by the CAD_{DBT} and CAD_{PPJ} systems at 1.87 and 2.42 FPs/view respectively. In an earlier study (Samala *et al.*, 2014b), we found that CAD_{PPJ} performed better than CAD_{DBT} for the 60°-21PV geometry. The current study showed that, for the 30°-11PV geometry, the performances of the two systems are comparable (fig. 9(b)). In fig. 10, the joint CAD results for the 30°-11PV test set were compared to those of the CAD_{DBT} and CAD_{PPJ} systems for the 60°-21PV test set. The dose for the 60°-21PV data set is approximately two times of that the 30°-11PV data set. Although the difference between the figures-of-merit in the JAFROC analysis of the joint-

CAD system for the 30°-11PV and the CAD_{PPJ} for the 60°-21PV did not achieve statistical significance, fig. 10 shows that at 85% sensitivity the FP rate of the 30°-11PV is more than twice that of the CAD_{PPJ} system. The final detection results for the 30°-11PV geometry are summarized in fig. 11; at a sensitivity of 85%, the FP rates are 0.49/view and 1.72/view from the case-based and view-based FROC curves, respectively. Figure 14 shows representative examples of some of the false negative clusters in the joint-CAD detection system. In example 3, the cluster was detected along the DBT path but the dynamic clustering did not form a cluster along the PPJ path and the DBT detected cluster was excluded by the decision tree classifier as FP. In example 4, the cluster was lost along the DBT path because its CNR was below the threshold (see section II.C.1). The cluster was detected on the PPJ path but was eventually excluded by the decision tree classifier. In example 5, the cluster was lost because the dynamic clustering failed to form a cluster due to too few calcification candidates for both the DBT and PPJ paths.

Advanced image analysis and visualization tools such as ‘synthetic’ image, slab view, computer-aided detection are expected to be widely used with DBT interpretation. CAD has the potential to improve radiologists’ accuracy and reduce reading time. Our case-based sensitivity of 90% at 1.04 FPs/view shows the potential for such applications. Studies have shown that combining information from the two views of each breast can further improve the performance of a CAD system (Sahiner *et al.*, 2006; van Schie *et al.*, 2011; van Engeland and Karssemeijer, 2007; Zheng *et al.*, 2006). The addition of ipsilateral detection to the joint-CAD system will be pursued in future studies.

The PPJ image is similar to a mammogram after removal of the structured tissue background and regularized high-frequency enhancement. For DBT systems that generate a synthetic 2-D mammogram from the DBT volume for radiologists’ reading, the synthetic mammogram is potentially useful either for augmenting or replacing the PPJ image in the joint-CAD system. However, if the synthetic mammogram is generated with the assistance of another CAD system (Van Schie *et al.*, 2013), the detection of lesions on such synthetic mammogram may be limited by the sensitivity of the original CAD system. Properly designed strategies have to be developed based on the characteristics of the available images in order to utilize effectively the joint information for lesion detection.

Our joint-CAD system achieved 85% sensitivity at 1.72 FPs/view for the data set with 30°-11PV geometry. The CAD system described by Reiser *et al* (Reiser *et al.*, 2008) reported 1.3 FPs/view at 86% sensitivity. Park *et al* (Park *et al.*, 2008) reported 70% sensitivity at 4 FPs/view and 88% sensitivity at 15.9 FPs/view for detection in PVs and DBT volume, respectively. Bernard *et al* (Bernard *et al.*, 2008) reported 1.7 FPs/view at 95% sensitivity. van Schie *et al* (van Schie and Karssemeijer, 2009) reported 1.5 FPs/view at 95% sensitivity. Wei *et al* (Wei *et al.*, 2014) reported 1.55 FPs/view at 90% sensitivity. Note that all these studies used data sets of different sizes with and without MCs, and the images were obtained with different DBT acquisition geometry, imaging techniques and dose, detector characteristics and reconstruction methods.

There are limitations in the current study. The 30°-11PV DBT geometry is close to the clinical systems commercially available or under development but we have not investigated

other narrow-tomographic angles with uniform or variable angular increments. The simulation of smaller or variable angular increments is not possible with our existing human subject data set. The MSBF-regularized SART reconstruction that we developed for the 60°-21PV DBT may not be optimal for the lower dose 30°-11PV DBT. It is important to further investigate if the regularization method may depend on the DBT acquisition geometry and whether the detection may be improved by further optimizing the regularization method for a specific geometry. Second, the data set size is limited and there are too few malignant clusters to analyze the performance difference between malignant and benign cases. Finally, we intended to train a CAD system to detect more suspicious MCs so that most of the malignant cases were allocated to the training set. The test set contained predominantly benign cases. Nevertheless, all cases in the test set had BI-RADS assessments of 4 or 5 that are the targets of interest for a CAD system for breast cancer screening. Furthermore, we believe that the test performance would not be optimistic because malignant clusters, on average, were detected with higher sensitivity than benign clusters as observed in previous studies (Scaranelo *et al.*, 2014; Ge *et al.*, 2007; Sahiner *et al.*, 2012; Bria *et al.*, 2014).

V. CONCLUSION

Noise is a major factor degrading the detection of subtle microcalcifications in the DBT volumes. We have shown that, for a relatively noisy DBT data set, combining detection in the reconstructed DBT volume and the PPJ image can increase the sensitivity while maintaining a reasonable FP rate. The joint-CAD approach significanlty outperforms individual CAD systems for detection in the DBT volume or the PPJ image alone and is comparable to the detection of MCs by the individual CAD systems using higher dose input images.

ACKNOWLEDGMENTS

This work is supported by USPHS grant RO1 CA151443. The digital breast tomosynthesis system was developed by the GE Global Research Group, with input and some revisions from the University of Michigan investigators, through the Biomedical Research Partnership (USPHS grant CA91713, PI: Paul Carson, Ph.D.) collaboration. The content of this paper does not necessarily reflect the position of the funding agency and no official endorsement of any equipment and product of any companies mentioned should be inferred.

References

Bernard S, Muller S, Onativia J. Computer-aided microcalcification detection on digital breast tomosynthesis data: A preliminary evaluation. IWDM 2008 - Lecture Notes in Computer Science. 2008; 5116:151–7.

Bria A, Karssemeijer N, Tortorella F. Learning from unbalanced data: A cascade-based approach for detecting clustered microcalcifications. Medical image analysis. 2014; 18:241–52. [PubMed: 24292553]

Chakrabarti, K.; Ochs, R.; Pennello, R.; Samuelson, F. [accessed on December 19, 2014] P080003 Hologic Selenia Dimensions 3D System. FDA Executive Summary. Sep. 2010 http://www.fda.gov/downloads/AdvisoryCommittees/CommitteesMeetingMaterials/MedicalDevices/MedicalDevicesAdvisoryCommittee/RadiologicalDevicesPanel/UCM226757.pdf

Chakraborty DP, Berbaum KS. Observer studies involving detection and localization: modeling, analysis, and validation. Medical Physics. 2004; 31:2313–30. [PubMed: 15377098]

Chan H-P, Goodsitt MM, Helvie M, Zelakiewicz S, Schmitz A, Noroozian M, Paramagul C, Roubidoux MA, Nees AV, Neal C, Carson P, Lu Y, Hadjiiski LM, Wei J. Digital breast tomosynthesis: Observer performance study of the detection of clustered microcalcifications in breast phantom images acquired with an experimental DBT system using variable scan angles, angular increments, and number of projection views. Radiology. 2014; 273:675–85. [PubMed: 25007048]

Chan H-P, Sahiner B, Lam KL, Petrick N, Helvie MA, Goodsitt MM, Adler DD. Computerized analysis of mammographic microcalcifications in morphological and texture feature space. Medical Physics. 1998; 25:2007–19. [PubMed: 9800710]

Ciatto S, Houssami N, Bernardi D, Caumo F, Pellegrini M, Brunelli S, Tuttobene P, Bricolo P, Fantò C, Valentini M, Montemezzi S, Macaskill P. Integration of 3D digital mammography with tomosynthesis for population breast-cancer screening (STORM): a prospective comparison study. The Lancet Oncology. 2013; 14:583–9. [PubMed: 23623721]

Food and Drug Administration. [accessed on May 22, 2015] MAMMOMAT Inspiration with Tomosynthesis Option - P140011. Apr. 2015 http://www.accessdata.fda.gov/cdrh_docs/pdf14/P140011a.pdf

Food and Drug Administration. [accessed on December 19, 2014] SenoClaire - P130020. Aug. 2014 http://www.accessdata.fda.gov/cdrh_docs/pdf13/P130020a.pdf

Ge J, Hadjiiski LM, Sahiner B, Wei J, Helvie MA, Zhou C, Chan H-P. Computer-aided detection system for clustered microcalcifications: comparison of performance on full-field digital mammograms and digitized screen-film mammograms. Physics in Medicine and Biology. 2007; 52:981–1000. [PubMed: 17264365]

Ge J, Sahiner B, Hadjiiski LM, Chan H-P, Wei J, Helvie MA, Zhou C. Computer aided detection of clusters of microcalcifications on full field digital mammograms. Medical Physics. 2006; 33:2975–88. [PubMed: 16964876]

Gurcan MN, Chan H-P, Sahiner B, Hadjiiski L, Petrick N, Helvie MA. Optimal neural network architecture selection: Improvement in computerized detection of microcalcifications. Academic Radiology. 2002; 9:420–9. [PubMed: 11942656]

Gurcan MN, Sahiner B, Chan H-P, Hadjiiski LM, Petrick N. Selection of an optimal neural network architecture for computer-aided detection of microcalcifications - comparison of automated optimization techniques. Medical Physics. 2001; 28:1937–48. [PubMed: 11585225]

Hall M, Frank E, Holmes G, Pfahringer B, Reutemann P, Witten IH. The WEKA data mining software: an update. ACM SIGKDD explorations newsletter. 2009; 11:10–8.

Lu Y, Chan H-P, Fessler JA, Hadjiiski L, Wei J, Goodsitt MM. Adaptive diffusion regularization for enhancement of microcalcifications in digital breast tomosynthesis (DBT) reconstruction. Proc. SPIE. 2011a; 7961:7961171–9.

Lu Y, Chan H-P, Wei J, Goodsitt MM, Carson PL, Hadjiiski L, Schmitz A, Eberhard JW, Claus BEH. Image quality of microcalcifications in digital breast tomosynthesis: Effects of projection-view distributions. Medical Physics. 2011b; 38:5703–12. [PubMed: 21992385]

Lu Y, Chan H-P, Wei J, Hadjiiski LM. Selective-diffusion regularization for enhancement of microcalcifications in digital breast tomosynthesis reconstruction. Medical Physics. 2010; 37:6003–14. [PubMed: 21158312]

Lu Y, Chan H-P, Wei J, Hadjiiski LM, Samala RK. Multiscale Bilateral Filtering for Improving Image Quality in Digital Breast Tomosynthesis. Medical Physics. 2015; 42:182–95. [PubMed: 25563259]

McCarthy AM, Kontos D, Synnestvedt M, Tan KS, Heitjan DF, Schnall M, Conant EF. Screening Outcomes Following Implementation of Digital Breast Tomosynthesis in a General-Population Screening Program. Journal of the National Cancer Institute. 2014; 106:dju316. [PubMed: 25313245]

Metz CE, Pan X. “Proper” binormal ROC curves: Theory and maximum-likelihood estimation. Journal of Mathematical Psychology. 1999; 43:1–33. [PubMed: 10069933]

Park SC, Zheng B, Wang XH, Gur D. Applying a 2D based CAD scheme for detecting microcalcification clusters using digital breast tomosynthesis images: An assessment - art. no. 691507. Proc. SPIE. 2008; 6915:6915071–8.

Plaisier SB, Taschereau R, Wong JA, Graeber TG. Rank–rank hypergeometric overlap: identification of statistically significant overlap between gene-expression signatures. Nucleic acids research. 2010; 38:e169–e. [PubMed: 20660011]

Poplack SP, Tosteson TD, Kogel CA, Nagy HM. Digital breast tomosynthesis: Initial experience in 98 women with abnormal digital screening mammography. American Journal of Roentgenology. 2007; 189:616–23. [PubMed: 17715109]

Quinlan, JR. C4.5: Programs for machine learning. Morgan Kaufmann; San Mateo, CA: 1993.

Reiser I, Nishikawa RM, Edwards AV, Kopans DB, Schmidt RA, Papaioannou J, Moore RH. Automated detection of microcalcification clusters for digital breast tomosynthesis using projection data only: A preliminary study. Medical Physics. 2008; 35:1486–93. [PubMed: 18491543]

Sahiner B, Chan H-P, Hadjiiski LM, Helvie MA, Paramagul C, Ge J, Wei J, Zhou C. Joint two-view information for computerized detection of microcalcifications on mammograms. Medical Physics. 2006; 33:2574–85. [PubMed: 16898462]

Sahiner B, Chan H-P, Hadjiiski LM, Helvie MA, Wei J, Zhou C, Lu Y. Computer-aided detection of clustered microcalcifications in digital breast tomosynthesis: A 3D approach. Medical Physics. 2012; 39:28–39. [PubMed: 22225272]

Samala RK, Chan H-P, Lu Y, Hadjiiski L, Wei J, Helvie M. Digital breast tomosynthesis: effects of projection-view distribution on computer-aided detection of microcalcification clusters. Proc. SPIE. 2014a; 9035:90350Y–Y-7.

Samala RK, Chan H-P, Lu Y, Hadjiiski L, Wei J, Helvie MA. Digital breast tomosynthesis: Computer-aided detection of clustered microcalcifications on planar projection images. Physics in medicine and biology. 2014b; 59:7457–77. [PubMed: 25393654]

Samala RK, Chan H-P, Lu Y, Hadjiiski LM, Wei J, Sahiner B, Helvie MA. Computer-aided detection of clustered microcalcifications in multiscale bilateral filtering regularized reconstructed digital breast tomosynthesis volume. Medical Physics. 2014c; 41:021901. [PubMed: 24506622]

Scaranelo A, Eiada R, Bukhanov K, Crystal P. Evaluation of breast amorphous calcifications by a computer-aided detection system in full-field digital mammography. Evaluation. 2014; 85

Sechopoulos I. A review of breast tomosynthesis. Part I. The image acquisition process. Medical physics. 2013; 40:014301. [PubMed: 23298126]

Skaane P, Bandos A, Gullien R, Eben E, Ekseth U, Haakenaasen U, Izadi M, Jebsen I, Jahr G, Krager M, Hofvind S. Prospective trial comparing full-field digital mammography (FFDM) versus combined FFDM and tomosynthesis in a population-based screening programme using independent double reading with arbitration. European Radiology. 2013a; 23:2061–71. [PubMed: 23553585]

Skaane P, Bandos AI, Gullien R, Eben EB, Ekseth U, Haakenaasen U, Izadi M, Jebsen IN, Jahr G, Krager M. Comparison of digital mammography alone and digital mammography plus tomosynthesis in a population-based screening program. Radiology. 2013b; 267:47–56. [PubMed: 23297332]

Spangler ML, Zuley ML, Sumkin JH, Abrams G, Ganott MA, Hakim C, Perrin R, Chough DM, Shah R, Gur D. Detection and Classification of Calcifications on Digital Breast Tomosynthesis and 2D Digital Mammography: A Comparison. American Journal of Roentgenology. 2011; 196:320–4. [PubMed: 21257882]

van Engeland S, Karssemeijer N. Combining two mammographic projections in a computer aided mass detection method. Medical Physics. 2007; 34:898–905. [PubMed: 17441235]

van Schie G, Karssemeijer N. Noise model for microcalcification detection in reconstructed tomosynthesis slices. Proc. SPIE. 2009; 7260:72600M1–M8.

Van Schie G, Mann R, Imhof-Tas M, Karssemeijer N. Generating synthetic mammograms from reconstructed tomosynthesis volumes. IEEE Transactions on Medical Imaging. 2013; 32:2322–31.

van Schie G, Tanner C, Snoeren P, Samulski M, Leifland K, Wallis MG, Karssemeijer N. Correlating locations in ipsilateral breast tomosynthesis views using an analytical hemispherical compression model. Physics in Medicine and Biology. 2011; 56:4715–30. [PubMed: 21737868]

Way T, Sahiner B, Hadjiiski L, Chan HP. Effect of finite sample size on feature selection and classification: a simulation study. Medical Physics. 2010; 37:907–20. [PubMed: 20229900]

Wei J, Chan H-P, Hadjiiski LM, Helvie MA, Lu Y, Zhou C, Samala RK. Multi-channel response analysis on 2D projection views for detection of clustered microcalcifications in digital breast tomosynthesis. Medical Physics. 2014; 41:041913. [PubMed: 24694144]

Xu N, Yi S, Mendonca P, Tian T-p, Samala R, Chan H-P. False positive reduction of microcalcification cluster detection in digital breast tomosynthesis. Proc. SPIE. 2014; 9034:90342N1–N7.

Zhang Y, Chan H-P, Sahiner B, Wei J, Goodsitt MM, Hadjiiski LM, Ge J, Zhou C. A comparative study of limited-angle cone-beam reconstruction methods for breast tomosynthesis. Medical Physics. 2006; 33:3781–95. [PubMed: 17089843]

Zheng B, Leader JK, Abrams GS, Lu AH, Wallace LP, Maitz GS, Gur D. Multiview-based computer-aided detection scheme for breast masses. Medical Physics. 2006; 33:3135–43. [PubMed: 17022205]

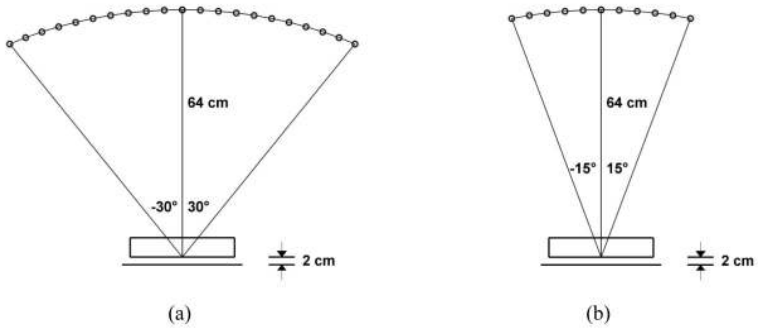

Fig. 1.

DBT acquisition geometry. (a) 60°-21PV: wide tomographic angle (60°) with 21 projections at 3° angular intervals. (b) 30°-11PV: simulated narrow tomographic angle (30°) with 11 projections at 3° angular intervals. The x-ray source motion is parallel to the chest wall. The distance between the x-ray focal spot and the fulcrum of the rotation is 64 cm (top surface of the breast support plate) with a spacing of 2 cm between the fulcrum and the image plane of the detector. The total focal-spot-to-detector distance is 66 cm.

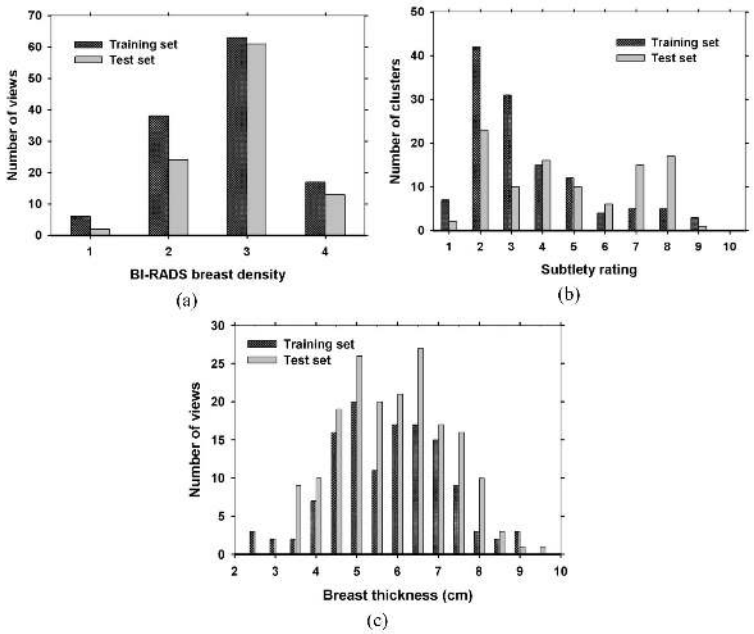

Fig. 2.

Characteristics of training and test data sets: (a) BI-RADS density and (b) subtlety ratings for breasts with MCs; a subtlety rating of 1 corresponds to the most visible cluster. (c) breast thickness for breasts with and without MCs.

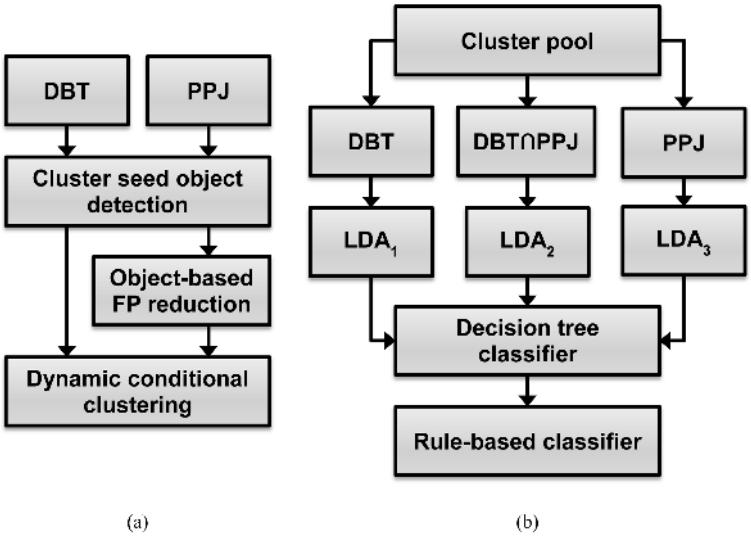

Fig. 3.

Schematic overview of the joint-CAD system: (a) cluster detection processes adapted from the individual CAD_{DBT} and CAD_{PPJ} systems. Note that the two processes are performed independently although some steps are shown with the same block in the schematic to illustrate the similarity. DBT: digital breast tomosynthesis reconstructed volume, PPJ: planar projection image. (b) joint FP reduction process after pooling the detected clusters from the two paths in (a). DBT and PPJ represent clusters from the CAD_{DBT} and CAD_{PPJ} systems, respectively, and LDA_i (i=1,2,3) are linear discriminant analysis classifiers trained for each path.

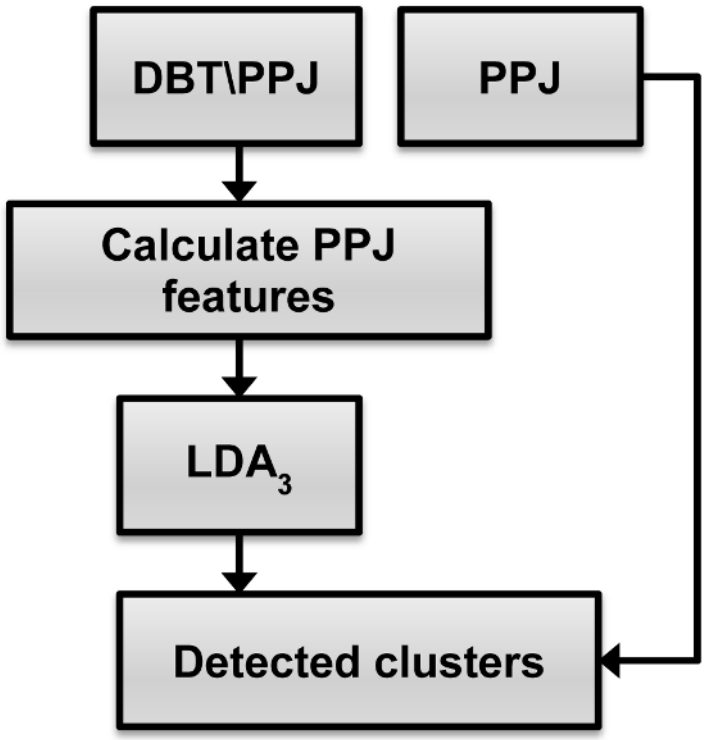

Fig. 4.
Mapping of clusters from the DBT path to the PPJ image. LDA_3: linear discriminant analysis classifier trained for PPJ clusters.

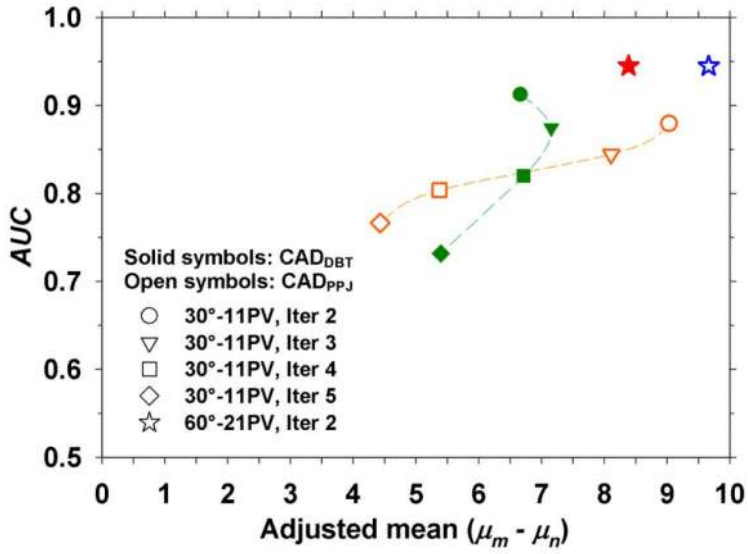

Fig. 5.

Figures-of-merit plot with adjusted mean on the x-axis and *AUC* on the y-axis. The dashed lines are drawn to facilitate following the change in the FOMs from iteration 2 to iteration 5. μ_m: mean CNR of the microcalcifications, μ_n: mean CNR of the FPs.

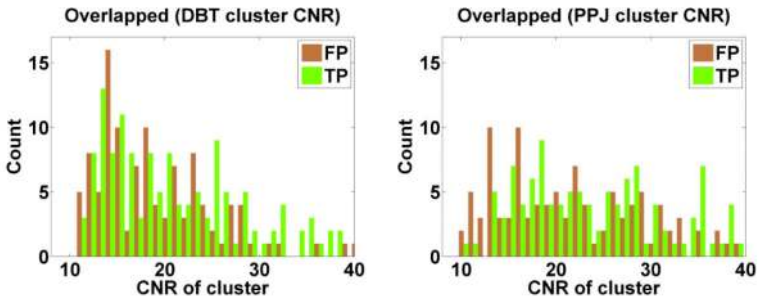

Fig. 6.

Histogram of overlapped clusters between the DBT and PPJ paths. The clusters shown are those obtained after the clustering stage in the respective paths. The TP and FP clusters are plotted in different colors. (left) DBT clusters with PPJ counterpart. (right) PPJ clusters with DBT counterpart.

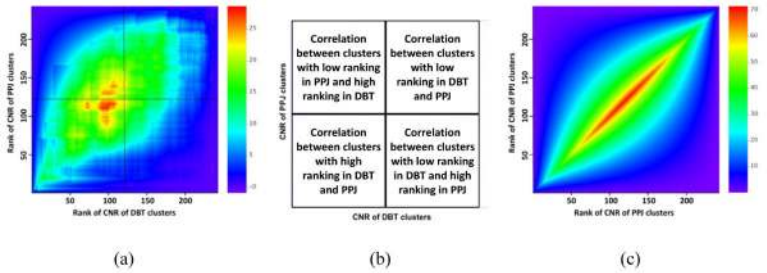

Fig. 7.

(a) RRHO distribution for overlapped clusters between the DBT and PPJ detection paths along x-axis and y-axis, respectively. The cross lines divide the map into different quadrants. (b) Interpretation of different quadrants in a RRHO distribution. (c) For illustration, an RRHO map where the clusters from the two paths have perfect correlation is simulated by using the clusters from PPJ path for both the x-axis and y-axis.

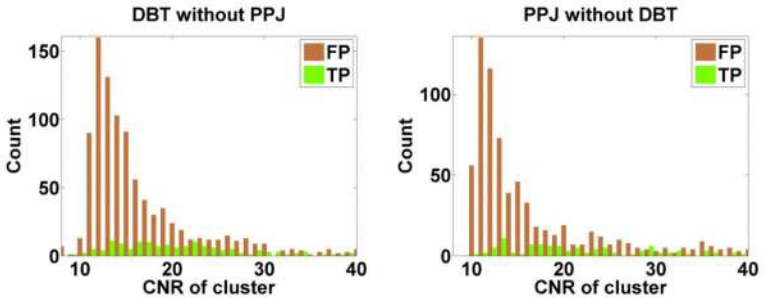

Fig. 8.

Histogram of non-overlapped clusters between the DBT and PPJ paths. The clusters shown are those obtained after the clustering stage in the respective paths. The TP and FP clusters are plotted in different colors. (left) DBT clusters without PPJ counterpart. (right) PPJ clusters without DBT counterpart.

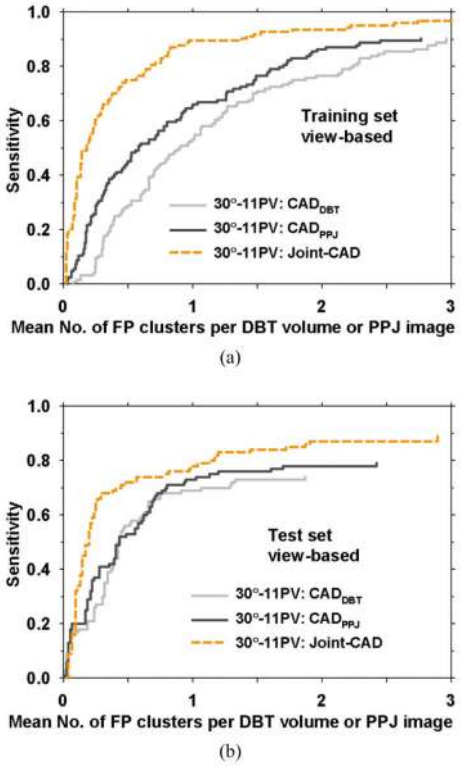

Fig. 9.

View-based FROC curves comparing the joint-CAD system with the CAD_{DBT} and CAD_{PPJ} systems in the 30°-11PV geometry. (a) Training results: the sensitivity was calculated relative to the 124 MCs in 127 views and the FP rate was estimated from the same set. (b) Test results: the sensitivity was calculated relative to the 100 MCs in 104 views and the FP rate was estimated from the 76 views without MCs. The differences between the joint-CAD curve and the CAD_{DBT} and CAD_{PPJ} curves are statistically significant ($p<0.05$) by JAFROC analysis (Table 4).

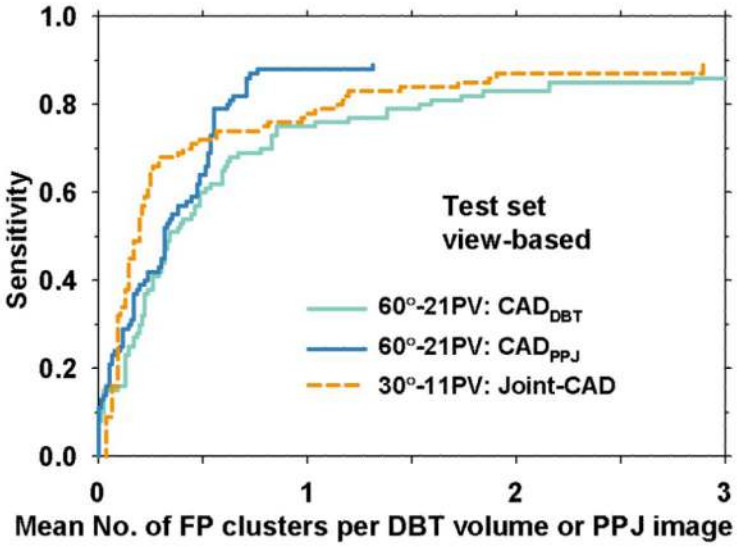

Fig. 10.

View-based FROC curves comparing the joint-CAD system for the test set in the 30°-11PV geometry with the CAD_{DBT} and CAD_{PPJ} systems for the same test set in the 60°-21PV geometry. The sensitivity was calculated relative to the 100 MCs in 104 views and the FP rate was estimated from the 76 views without MCs. The differences between the joint-CAD curve and the 60°-21PV curves did not achieve statistical significance by JAFROC analysis ($p>0.05$).

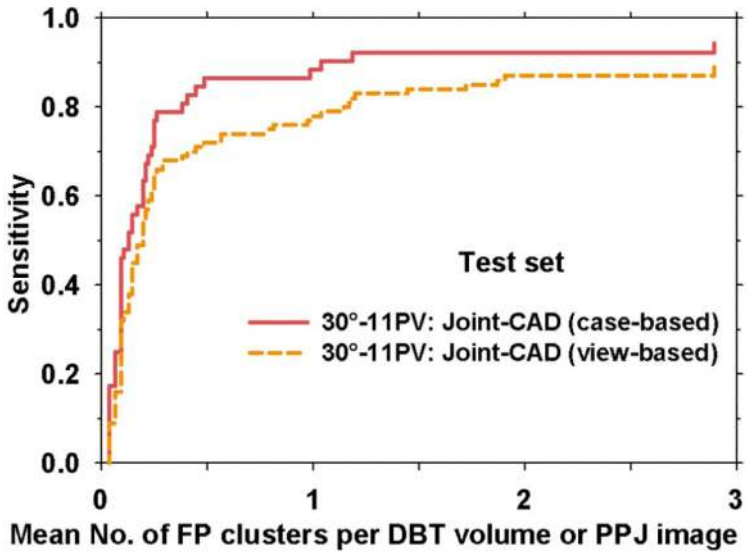

Fig. 11.

Case-based and view-based FROC curves of the joint-CAD system for the test set in the 30°-11PV geometry. The viewed-based sensitivity was calculated from the 104 views with MCs and the case-based sensitivity was calculated relative to the 52 breasts with MCs. The FP rate was estimated from the 76 views without MCs.

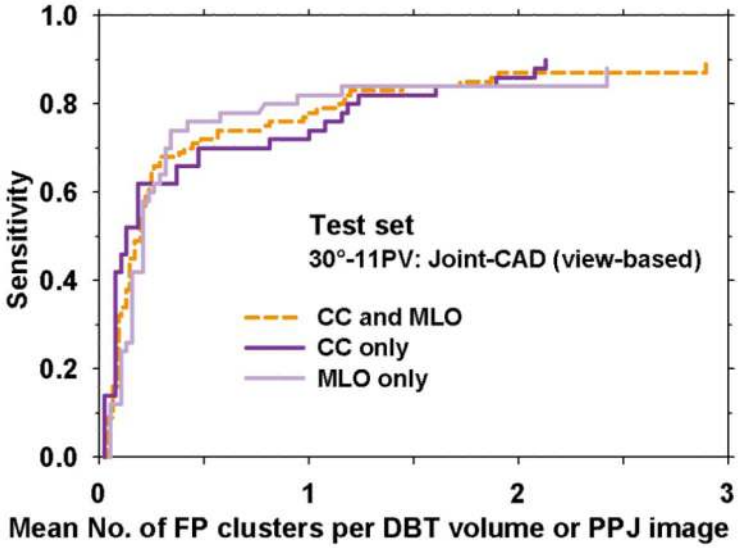

Fig. 12.

View-based FROC curves of the joint-CAD system for the test set in the 30°-11PV geometry for all views compared to FROC curves for CC views only and MLO views only in the same test set. For the CC-only and MLO-only curves, the viewed-based sensitivity was calculated from the 52 views with MCs and the FP rate was estimated from the 38 corresponding views without MCs. The difference between the FROC curves for CC only and MLO only did not achieve statistical significance by JAFROC analysis ($p>0.05$).

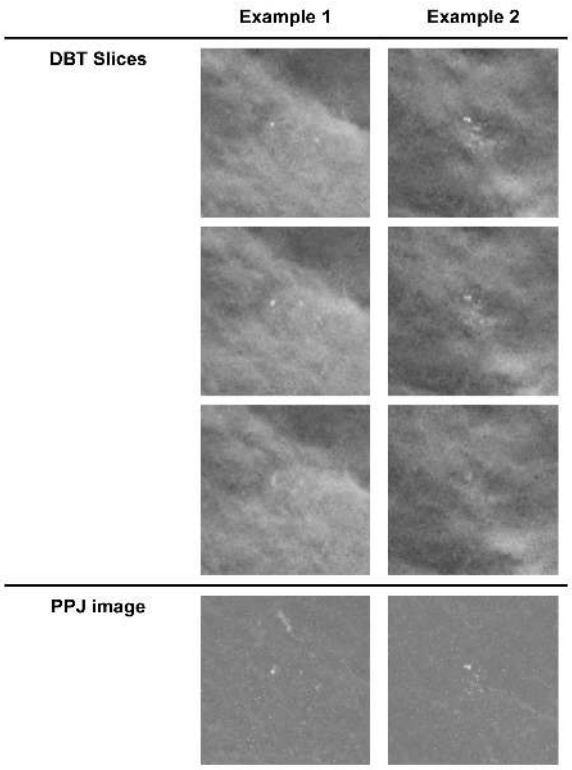

Fig. 13.

Examples of regions of interest showing clusters in consecutive DBT slices and the corresponding PPJ image. All ROIs are 15 × 15 mm (150 × 150 pixels). Example 1 (slices 50-52) is biopsy-proven to be ductal carcinoma in situ with the MC detected only on the DBT path of the joint-CAD system. Example 2 (slices 49-51) is fibrocystic disease detected on the PPJ path of the joint-CAD system. Both clusters were detected at the final stage of the joint-CAD system.

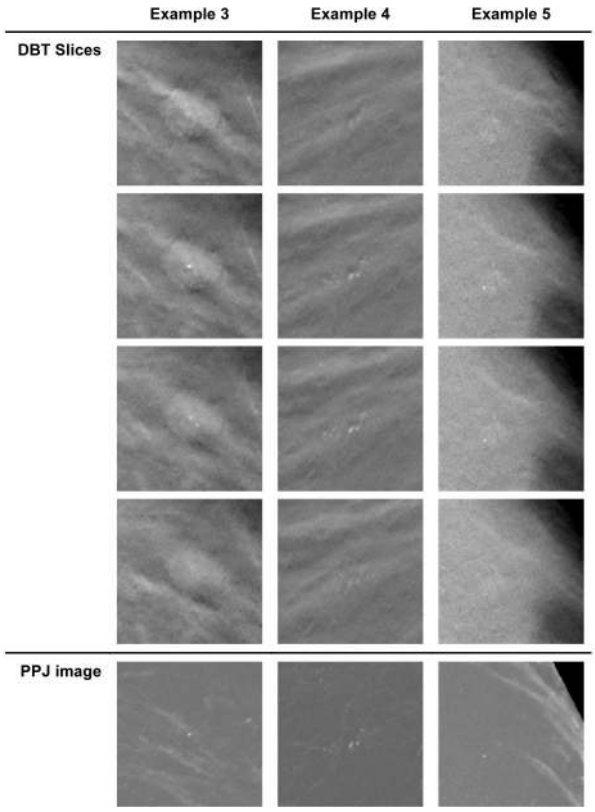

Fig. 14.

Examples of regions of interest showing clusters in consecutive DBT slices and the corresponding PPJ image. All ROIs are 15 × 15 mm (150 × 150 pixels). Example 3 (slices 42-45) is biopsy-proven to be pseudoangiomatous stromal hyperplasia with the MC detected only on the DBT path, no detection on the PPJ path and lost at the decision tree classification stage. Example 4 (slices 35-38) is fibrocystic disease detected on the PPJ path, no detection on the DBT path and lost at the decision tree classification stage. Example 5 (slices 44-47) is biopsy-proven to be ductal carcinoma in situ with the MC lost on both the DBT and PPJ paths.

Table 1

Comparison of DBT characteristics between the training and test sets. The numbers shown are by view.

Characteristic	Training Set	Test Set
Number of views (CC/MLO)	127 (63/64)	180 (90/90)
Benign MCs	62	102
Malignant MCs (in situ/ invasive cancers)	65 (51/14)	2 (2/0)
No MCs (CC/MLO)	0	76 (38/38)
Mean age (range)	52.3±9.8 (42.5 to 62.1)	50.9±8.1 (42.8-59)
Breast thickness (cm)	5.8±1.4 (2.3-9)	5.9±1.3 (3.5-9.5)

Table 2

Analysis of TPs and FPs from the training set after different stages of the joint-CAD system. Sensitivity is calculated relative to 124 clusters in the 127 views. FP reduction is calculated relative to the total number of cluster candidates from the three paths after the prescreening stage.

Detection stage	FP reduction	False negative	Sensitivity
Prescreening	NA	0.8%	99.2%
Decision tree classifier	70.9%	1.6%	97.6%
Rule-based classifier	7.1%	0%	97.6%

Table 3

Mean number of FP clusters per DBT volume or PPJ image at several sensitivities from the FROC curve of the joint-CAD system for the 30°-11PV test set.

Sensitivity	Mean number of FPs per DBT volume or PPJ image	
	View-based	Case-based
60%	0.24	0.20
70%	0.41	0.24
75%	0.79	0.25
80%	1.14	0.38
85%	1.72	0.49

Table 4

JAFROC analysis comparing the performances between the joint-CAD and the CAD_{DBT} and CAD_{PPJ} for the test set in the 30°-11PV geometry (fig. 9(b)). The asterisk * indicates that the difference in the figure-of-merit (FOM) was statistically significant at the $p<0.05$ level. CI: confidence interval.

CAD	FOM	CI
Joint-CAD	0.62	(0.54, 0.69)
CAD_{DBT}	0.53	(0.46, 0.60)
p value		0.0036*
Joint-CAD	0.62	(0.54, 0.69)
CAD_{PPJ}	0.54	(0.47, 0.61)
p value		0.034*